SCIENTIFIC REPORTS

OPEN

Received: 10 June 2016
Accepted: 07 September 2016
Published: 27 September 2016

Fabrication of potato-like silver molybdate microstructures for photocatalytic degradation of chronic toxicity ciprofloxacin and highly selective electrochemical detection of H_2O_2

J. Vinoth Kumar[1], R. Karthik[2], Shen-Ming Chen[2], V. Muthuraj[1] & Chelladurai Karuppiah[2,3]

In the present work, potato-like silver molybdate (Ag_2MoO_4) microstructures were synthesized through a simple hydrothermal method. The microstructures of Ag_2MoO_4 were characterized by various analytical and spectroscopic techniques such as XRD, FTIR, Raman, SEM, EDX and XPS. Interestingly, the as-prepared Ag_2MoO_4 showed excellent photocatalytic and electrocatalytic activity for the degradation of ciprofloxacin (CIP) and electrochemical detection of hydrogen peroxide (H_2O_2), respectively. The ultraviolet-visible (UV-Vis) spectroscopy results revealed that the potato-like Ag_2MoO_4 microstructures could offer a high photocatalytic activity towards the degradation of CIP under UV-light illumination, leads to rapid degradation within 40 min with a degradation rate of above 98%. In addition, the cyclic voltammetry (CV) and amperometry studies were realized that the electrochemical performance of Ag_2MoO_4 modified electrode toward H_2O_2 detection. Our H_2O_2 sensor shows a wide linear range and lower detection limit of 0.04–240 μM and 0.03 μM, respectively. The Ag_2MoO_4 modified electrode exhibits a high selectivity towards the detection of H_2O_2 in the presence of different biological interferences. These results suggested that the development of potato-like Ag_2MoO_4 microstructure could be an efficient photocatalyst as well as electrocatalyst in the potential application of environmental, biomedical and pharmaceutical samples.

Nowadays, antibiotics are main class of antimicrobial drugs in today's medicine and widely used to prevent the bacterial infection for both human and animals. In particular, ciprofloxacin (CIP), as an antibiotic drug, plays an important role for the treatment of urinary, digestive infections and pulmonary diseases[1]. The CIP can be entered into the aquatic environment through the intentional disposal of surplus drugs, the release of excreta from human and animals, malapropos treatment in the hospitals or in pharmaceutical industries, improper removal of waste water treatment plants and the use of animal's feces as agricultural fertilizers[2,3]. Probably, the CIP drug is not completely metabolized and the continuous release of CIP into the environments displays the chronic toxicity to bacteria, which causes toxicity to the microorganism and retarding to aquatic vertebrates[4,5]. It also interacts with photosynthesis process and inhibits the growth of spinach plants[6] and cause antibiotic-resistance bacteria growth in the environment[7]. Therefore, the removals of CIP from the water sources are major concern to protect the aquatic system and soil environment. Several methods have been reported for the removal of CIP from water including adsorption[8], oxidation[9], sonolysis[10], sorption[11], (photo)-Fenton process[12], photocatalytic degradation[13–15] and ozonation[16]. Among them, photocatalysis is an efficient, cost-effective and eco-friendly method

[1]Department of Chemistry, VHNSN College, Virudhunagar–626001, Tamilnadu, India. [2]Department of Chemical Engineering, National Taipei University of Technology, No. 1, Section 3, Chung-Hsiao East Road, Taipei 106, Taiwan, ROC. [3]Department of Chemistry, National Taiwan University, No. 1, Sec. 4, Roosevelt Rd, Daan District, Taipei, Taiwan-10617. Correspondence and requests for materials should be addressed to S.-M.C. (email: smchen78@ms15.hinet.net) or V.M. (email: muthuraj75@gmail.com)

for the environmental remediation, which degrades the hazardous organic pollutants into easily bio-degradable or nontoxic molecules[17,18].

On the other hand, hydrogen peroxide (H_2O_2) is an essential intermediate in the various food manufacturing and also involved in our life process. The detection of H_2O_2 is a paramount issue because it is a major reactive oxygen species, generated by most oxidases in mitochondria and related to the several bodily disorders such as myocardial infarction, atherosclerosis, and Alzheimer's disease, cancer, etc.[19]. H_2O_2 is also acts contrarily in cell growth, differentiation, physiological signaling pathways, migration and immune function system[20]. Moreover, it is most significant chemical in clinical, pharmaceutical industries and atomic power stations, which dramatically have an effect on the cloud and rainwater[21] as well as a precursor to the formation of more reactive and potentially harmful hydroxyl radicals[22]. Therefore, the trace level detection of H_2O_2 is an important concern for the environment and medicinal fields. Up to now, various methods are available to detect the H_2O_2 and some of them have been explored a satisfactory results to the concern of H_2O_2 detection[23]. However, the electrochemical methods hold more advantages such as simplicity, portability, rapid analysis, high sensitivity and low-cost instrumentation. Due to these attractive features, the electrochemical methods are represent a promising alternative technique for the determination of H_2O_2.

Transition metal-based molybdates (M = Fe, Ni, Co, Ag, Mn etc.,) are considered as an important inorganic material which are widely explored in different applications such as Li-ion storage batteries[24], birefringent filters[25], supercapacitors[26,27], optical fibers[28], photoluminescence[29], scintillation crystal[30], photocatalyst[31,32], humidity sensors[33], magnetic properties[34] and catalysts[35]. However, low dimensional metal molybdates have attracted more curiosity in current years. In particular, silver molybdate (Ag_2MoO_4) has attracted considerable attention because of its unique properties such as environmental friendly, photoluminescence, high electrical conductivity, excellent antimicrobial activity, good photocatalytic activity and remarkable electrochemical energy storage performance[36]. Due to these properties, the Ag_2MoO_4 is potentially used in several applications including ion-conducting glasses[37], high-temperature lubrication[38], gas sensor[39], antibacterial material[40], photoswitches[41] and ceramics[42]. In photocatalysis, Ag_2MoO_4 has paid significant attention owing to it's photosensitivity which make this material with high photocatalytic activity under UV or visible-light irradiation. Recently, few kinds of literature are reported based on Ag_2MoO_4 and its composite that act as a photocatalyst for the degradation of organic dyes into the wastewater[43–45]. The photocatalytic activity mainly depends on the crystal and electronic structures of materials that affect the energy band structure and the efficiency of charge carrier transfer. Moreover, to improve their physicochemical properties of the photocatalyst, researchers have growled a number of approaches to obtain the different morphologies of Ag_2MoO_4 including nanoparticles, nanorods, nanowires, wire-like nanostructures, nanoclusters, broom-like, flower-like microstructures and microcrystals[36,41,46–50]. However, to the best of our knowledge, we reported the synthesis of potato-like Ag_2MoO_4 microstructure, its applications for the photocatalytic degradation of CIP and electrochemical detection of H_2O_2 for the first time.

In this present work, we developed a simple one-pot hydrothermal synthesis of potato-like Ag_2MoO_4 microparticles with the assistance of urea and characterized using various analytical and spectroscopic techniques in detailed and further evaluated for electrochemical sensing and photocatalytic applications, as illustrated Fig. 1. Fascinatingly, we find that the as-prepared potato-like Ag_2MoO_4 microparticles exhibited a high-performance electrochemical sensor for the detection of H_2O_2. Moreover, their photocatalytic activity towards the removal of CIP antibiotic into the environment was also investigated with efficient degradation rate.

Results and Discussion

The crystalline structure and phase purity of the as-synthesized samples were determined by using XRD pattern as shown in Fig. 2A. The distinctive diffraction peaks obtained at 16.48°, 27.09°, 31.87°, 33.31°, 38.65°, 42.27°, 47.84°, 50.93°, 55.81°, 63.10°, 65.70°, 66.57°, 76.49° and 78.90° in the 2θ range which well agreed to the (111), (220), (311), (222), (400), (331), (422), (511), (440), (620), (533), (622), (642) and (731) reflection planes, respectively. Aforementioned planes are well related to the standard XRD report of cubic phase structured Ag_2MoO_4 with the space group of $Fd\bar{3}m$[51]. From the XRD pattern, it was clearly revealed that the as-synthesized product is β-Ag_2MoO_4[36]. The appearance of sharp and high intense peaks demonstrated the higher crystalline nature of cubic Ag_2MoO_4 phase. There is no any other peaks were appeared which related to the Ag_2O or MoO_3 phase, indicates the as-synthesized Ag_2MoO_4 was homogeneous solid.

FTIR and Raman spectroscopy is an important tool for analyzing the involvement of functional groups present in the as-synthesized Ag_2MoO_4. In the FTIR spectra (Fig. 2B), the absorption peaks at 3280 and 1650 cm^{-1} correspond to the O-H stretching and bending vibrations of the water molecules, respectively[52]. The peak at 645 cm^{-1} is confirmed the Ag-O stretching vibration of Ag_2MoO_4. The sharp peak at 891 cm^{-1} attributed to the anti-symmetric Mo-O stretching in tetrahedral MoO_4^{2-} ion[53]. Raman spectra showed (Fig. 2C) the peaks at 896, 782, 382 and 305 cm^{-1} which are due to the ν_1 (A_g), ν_3 (E_g), ν_4 (B_g) and ν_2 (A_g) symmetric and asymmetric stretching vibration modes of Ag_2MoO_4, respectively. The vibration modes at 896 and 782 cm^{-1} could be ascribed to the symmetric stretching vibration of Mo-O bond of the MoO_4 unit and the asymmetric stretching vibrations of the molybdate ion, respectively. The peaks at 382 and 305 cm^{-1} were clearly indicated the ν_4 and ν_2 bending vibration modes of tetrahedral MoO_4[54].

The surface morphology of the as-prepared microstructures was investigated by SEM. Figure 3(A–C) illustrated the general views of the different magnifications of the obtained Ag_2MoO_4 microstructures. The images are clearly displayed the potato-like structure of Ag_2MoO_4 which seems like bunches of potatoes with clean and fairly smooth surfaces, the average diameters of microstructures about 1–2 μm. Energy dispersive x-ray spectra (EDX) were used to identify the elements present in the as-prepared Ag_2MoO_4 microparticles, as depicted in Fig. 3D. The EDX spectra showed the peaks at approximately 0.5, 2.4 and 3 keV reveal the presence of O, Mo, and Ag elements in the material without any other significant impurities.

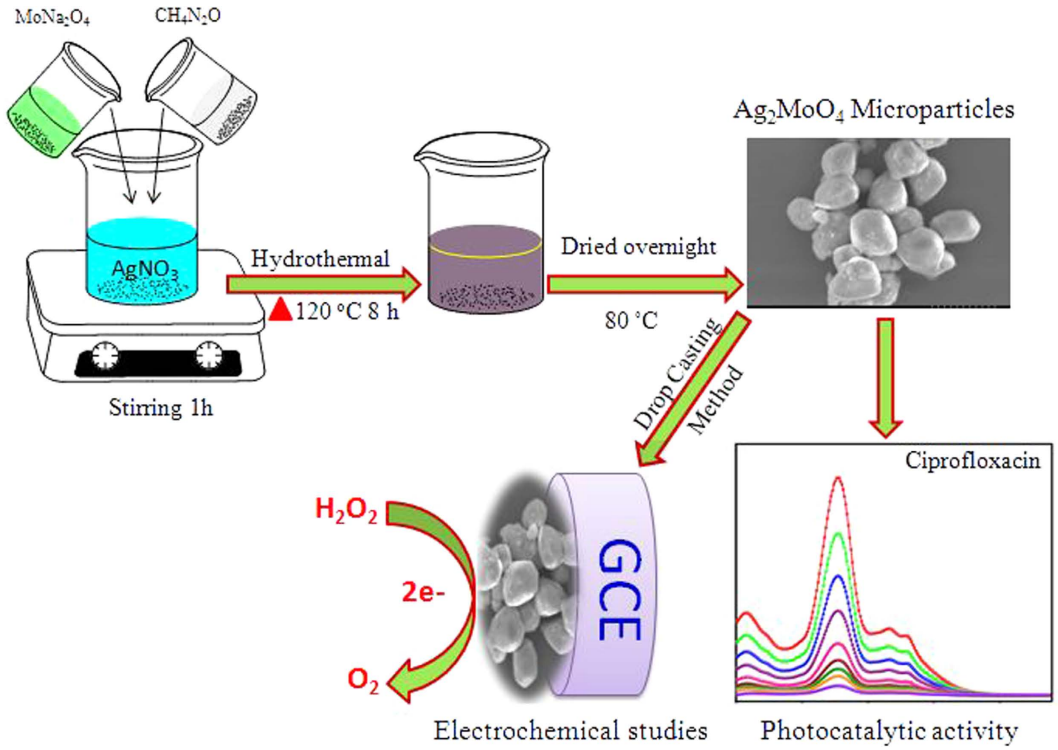

Figure 1. The synthesis route for Ag_2MoO_4 microparticles and its application for photocatalytic activity and electrochemical biosensor.

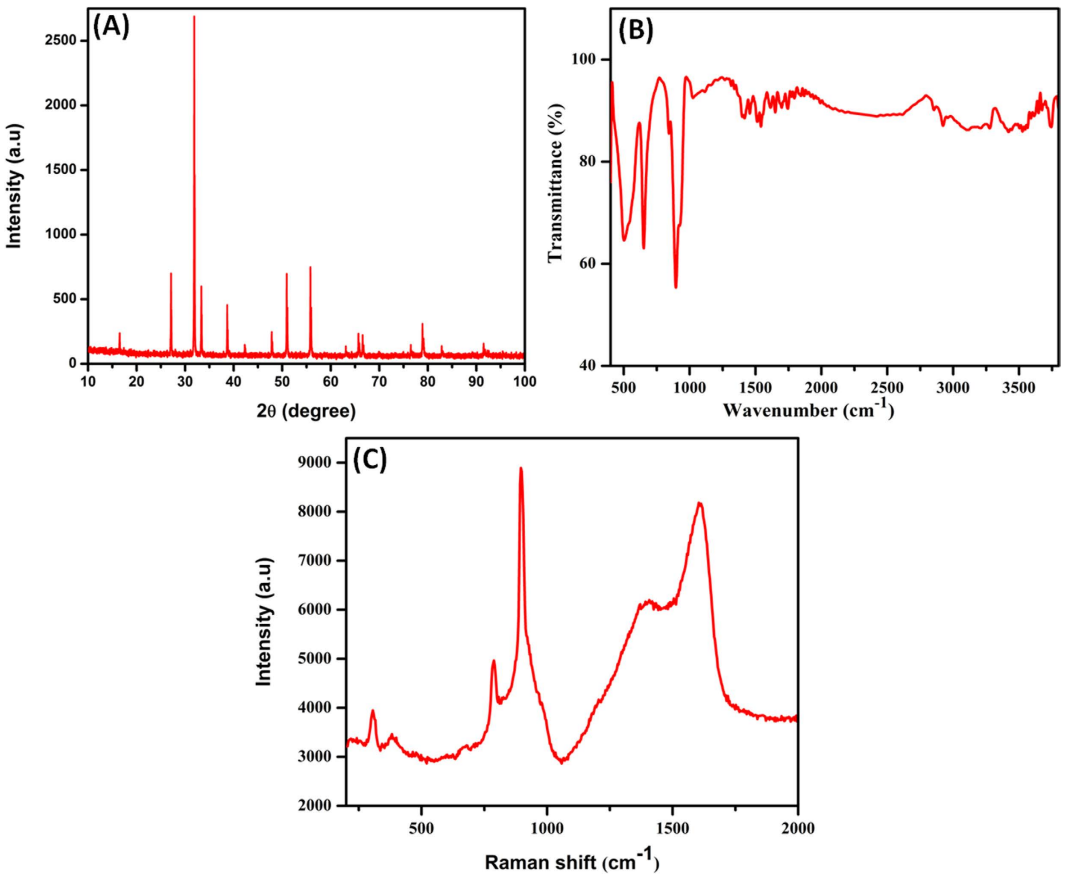

Figure 2. (**A**) XRD patterns (**B**) FTIR spectra and (**C**) Raman spectra of as-prepared Ag_2MoO_4.

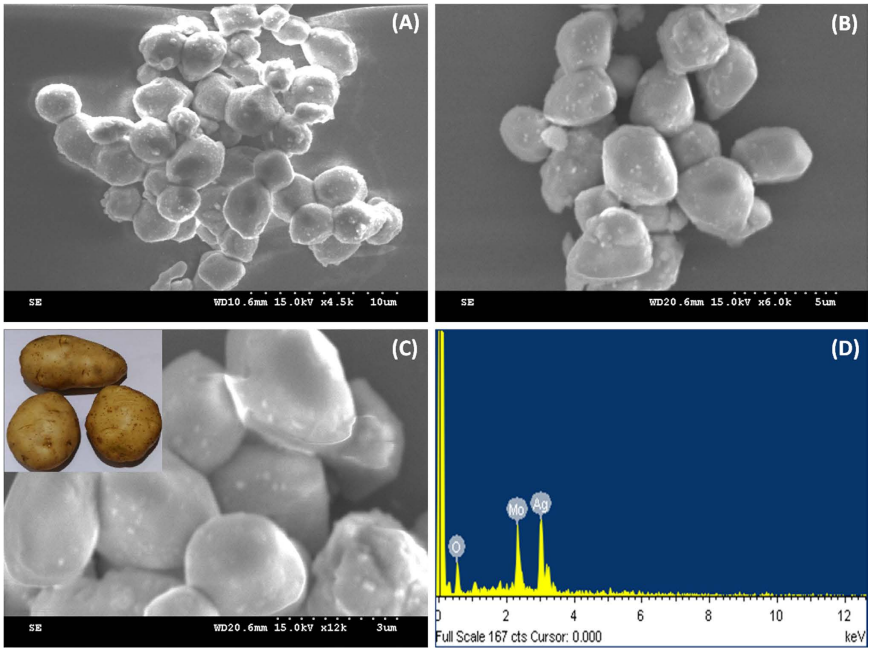

Figure 3. (**A–C**) SEM images of Ag_2MoO_4 at different magnifications (**A**) 10 μm (**B**) 5 μm (**C**) 3 μm and (**D**) corresponding to EDX spectrum of Ag_2MoO_4.

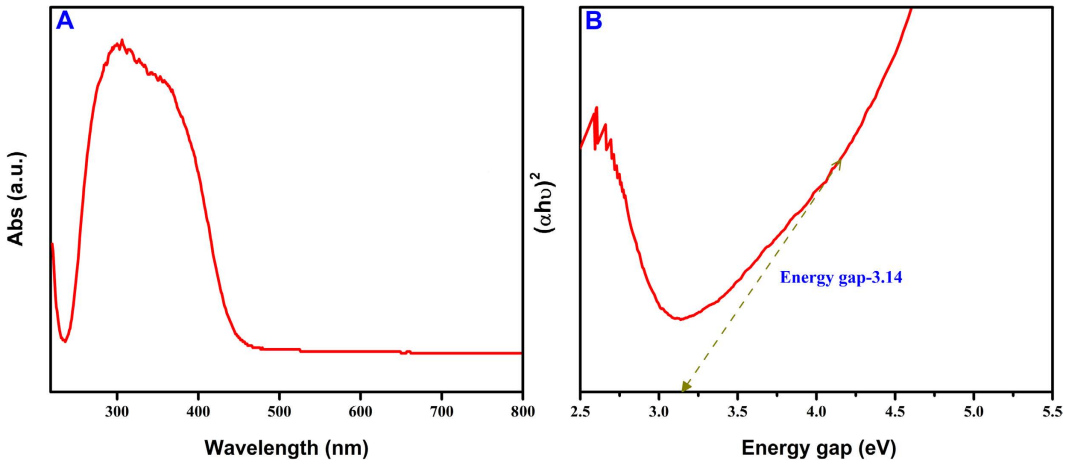

Figure 4. (**A**) UV-Vis diffuse reflectance spectra (DRS) and (**B**) Energy gap spectra of Ag_2MoO_4.

The bandgap energy of the Ag_2MoO_4 is an important parameter for the selection of suitable kind of light source needed for the degradation purposes. The UV-Vis (Diffuse reflectance) absorption spectrum of Ag_2MoO_4 microparticles is shown in Fig. 4A. The results shows that the relation between the normalized absorption of the photocatalyst and wavelength with a range of 200–800 nm. The most part of absorption spectra of Ag_2MoO_4 falls in the UV region, a broad steep from 300 to 420 nm which corresponds to the band gap energy value from 3–3.34 eV. The band gap value was calculated using Tauc's equation and the graph plotted $(\alpha h\nu)^2$ against $(h\nu)$ as can be seen in Fig. 4B. The calculated band gap energy value is 3.14 eV. On the other hand, the bandgap of Ag_2MoO_4 is significantly altered compared to that of previous reports[36,43,44,50]. The oxygen vacancy created in the crystal lattice of the Ag_2MoO_4 is leads to the distortion in the energy levels and influenced the bandgap which may be attributed to the effect of hydrothermal environment on the surface microstructures.

X-ray photoelectron spectroscopy (XPS) was used to evaluate the information about the chemical composition and chemical status of the as-synthesized Ag_2MoO_4, as shown in Fig. 5. The overall XPS spectrum in Fig. 5A shows the coexistence of elements Mo, C, Ag and O within the as-prepared Ag_2MoO_4 microparticles and no other impurities were detected, which are in good agreement with EDX report. In addition, the presence of C peak at 284.9 eV is ascribed to the adventitious hydrocarbon from the XPS instrument and it is inherent. High resolution scanning XPS spectra clearly confirms the Ag 3d, Mo 3d, and O 1s level, which is fitted by using the Gaussian fitting method, as shown in Fig. 5(B–D). In Fig. 5B, the Ag 3d spectra displays the two peaks at 368.7 and 374.4 eV

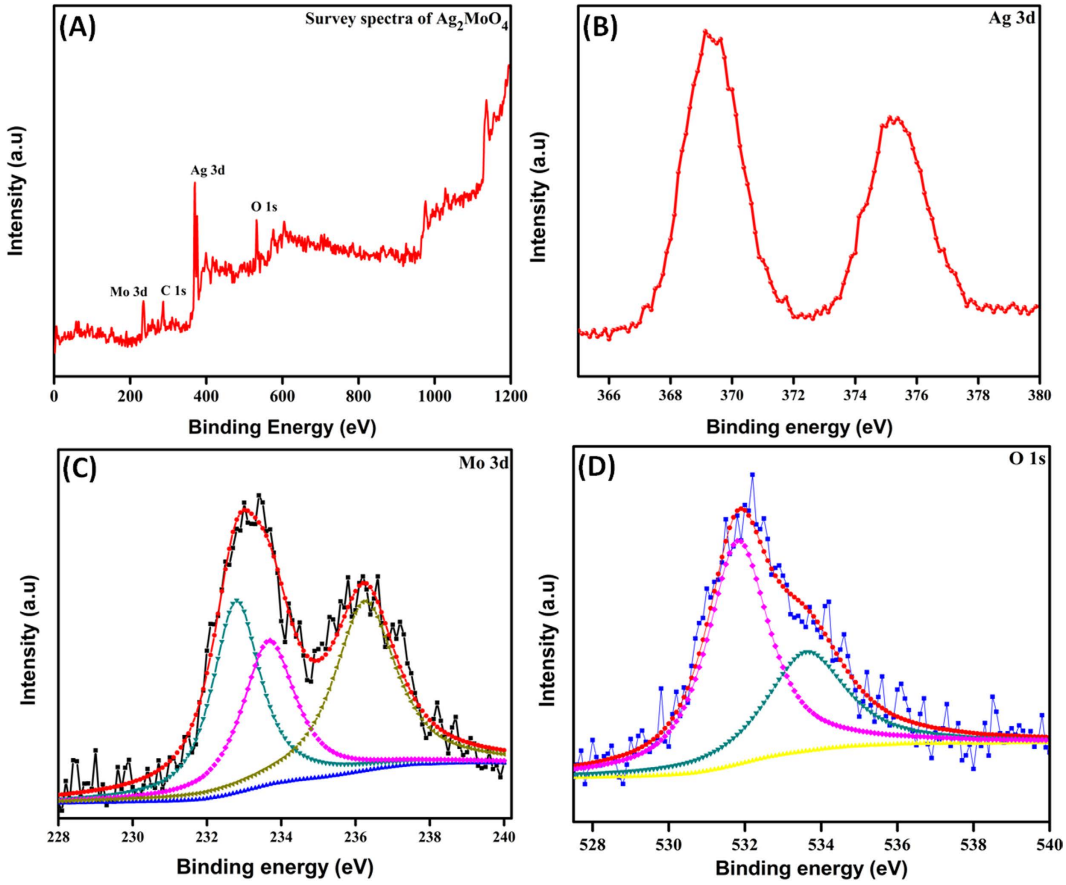

Figure 5. (**A**) XPS survey spectra of Ag_2MoO_4, (**B–D**) High resolution XPS spectra of Ag 3d, Mo 3d and O 1s.

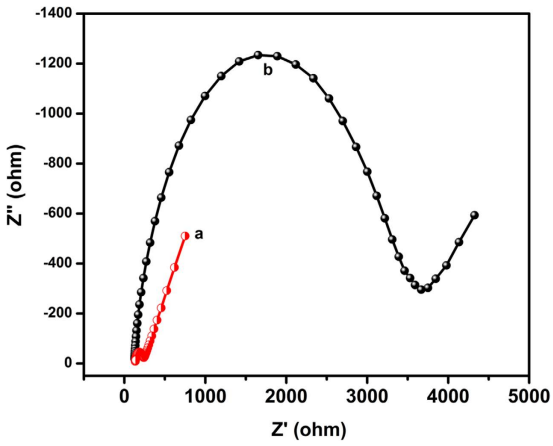

Figure 6. Electrochemical impedance spectroscopy of different modified electrodes (**a**) bare GCE (**b**) Ag_2MoO_4 modified GCE in 0.1 M KCl solution containing 5 mM $[Fe(CN)_6]^{3-/4-}$.

attributed to the Ag $3d_{5/2}$ and Ag $3d_{3/2}$ electron binding energy in Ag_2MoO_4, respectively[55]. The peaks at 233.2 and 236.3 eV ascribed to the Mo $3d_{5/2}$ and Mo $3d_{3/2}$ binding energy of Mo 3d, respectively. The major binding energy peaks Mo $3d_{5/2}$ and Mo $3d_{3/2}$ are separated by 3.1 eV, which belongs to the Mo^{6+} oxidation state as depicted in Fig. 5C[56]. The high intense peaks at around in the range of 530.5–533.6 eV revealed the presence of O 1s core level[57] in Ag_2MoO_4 (Fig. 5D). Hence, the obtained XPS results clearly confirmed that the valence of Ag, Mo and O are +1, +6 and −2, respectively, which is very good agreement with the phase structure of Ag_2MoO_4.

Electrochemical impedance spectroscopy (EIS) was used to investigate the changes of the electrode surface during the fabrication process. The nyquist curves of the EIS spectra was observed using bare GCE (a) and Ag_2MoO_4 modified GCE (b) in 0.1 M KCl containing 5.0 mM $K_3Fe(CN)_6/K_4Fe(CN)_6$ (Fig. 6). The diameter of

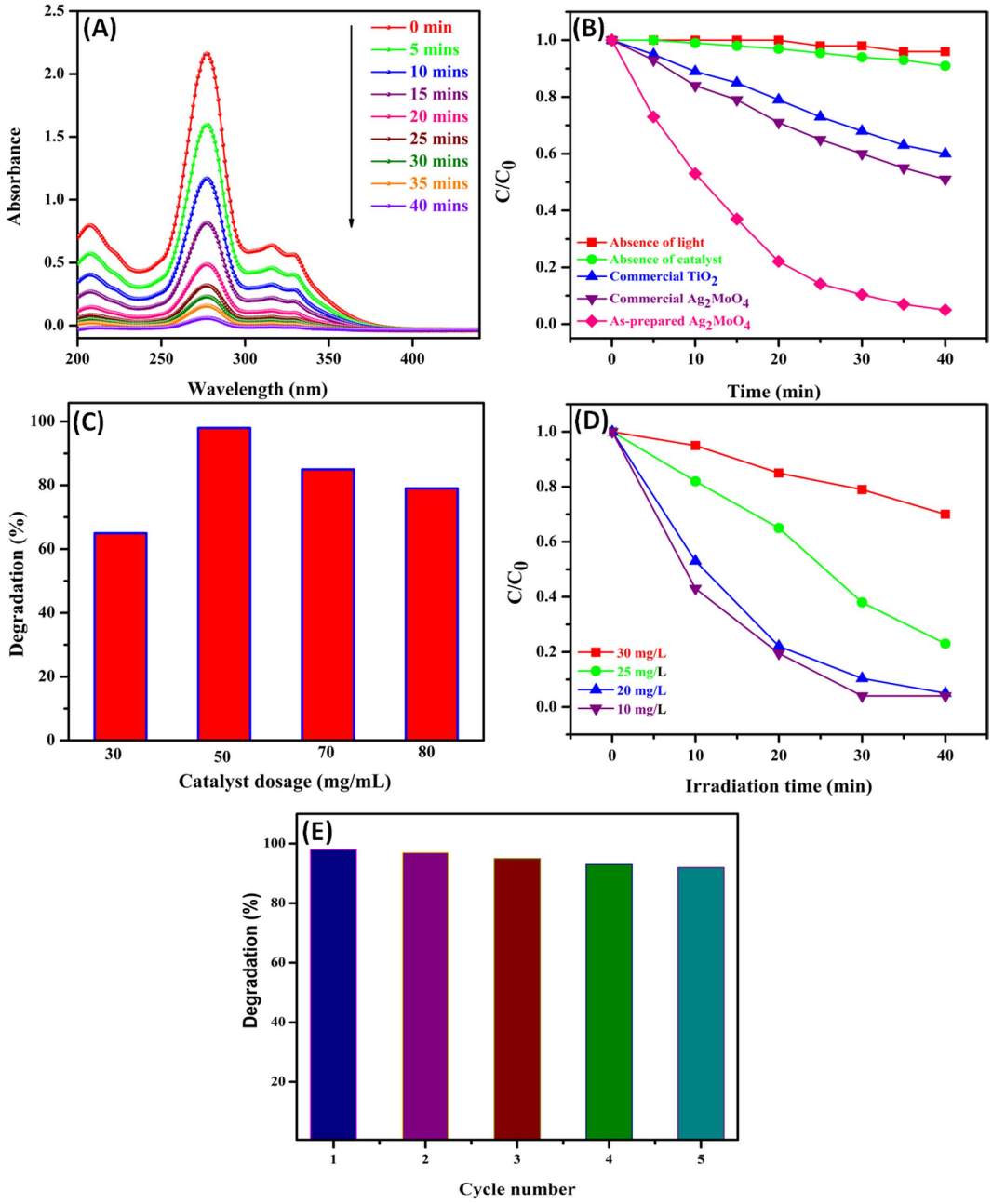

Figure 7. (**A**) Absorption spectrum of CIP in the presence of 50 mg/mL Ag_2MoO_4 under UV-light illumination. (**B**) Photodegradation of CIP in the presence of different catalysts. (**C**) Effect of catalyst amount dosage on the photodegradation of CIP. (**D**) Effect of initial CIP concentration on the photodegradation and (**E**) reusability of the potato-like Ag_2MoO_4 photocatalyst.

the semicircle indicates the electron transfer resistance (R_{ct}) of the electrode. This resistance controls the electron transfer kinetics of redox probe at the electrode interface. From the EIS results, the Ag_2MoO_4 modified GCE (b) shows larger semicircle than bare GCE (a) reveals that the Ag_2MoO_4 modified GCE can increase the electron transfer resistance on electrode surface, because it is hindered the electron transfer of $K_3Fe(CN)_6/K_4Fe(CN)_6$, thus confirming the successful modification of Ag_2MoO_4 on the GCE surface.

Photocatalytic activity. The photocatalytic behavior of as-prepared Ag_2MoO_4 microparticles was performed against the degradation of CIP under UV-light illumination, as illustrated in Fig. 7A. The absorbance spectrum shows the progressive degradation of CIP and the main absorption peak of CIP was observed at 276 nm and other small peaks were also completely diminished within 40 min. The degradation percentage of CIP solution was estimated from the relative intensity of absorbance in UV-visible spectra. The relative intensity of absorbance was decreased and reached almost zero within 40 min, reveals that the Ag_2MoO_4 microparticles degraded the 98% of the CIP solution. Initially, the utmost decrement of CIP was observed which could be attributed to

the competence of CIP with hydroxyl radicals generated by UV-light photoexcitation of Ag_2MoO_4 microparticles. However, as the reaction proceeds, the formation of by-products from degradation might compete with the hydroxyl radicals and adsorption sites on the catalyst surface. Hence, the gradual degradation of CIP was observed.

Under similar degradation conditions, commercially available Ag_2MoO_4 and commercial TiO_2 powder were also employed as a photocatalyst and their accurate comparison was carried out which depicted in Fig. 7B. The photocatalytic activity of commercial Ag_2MoO_4 and TiO_2 on CIP degradation exhibited a poor efficiency and the corresponding degradation percentages are observed around 38% and 32%, respectively. Moreover, there is no significant degradation was observed either in the absence of light or in the absence of a catalyst. The results clearly confirmed the as-synthesized Ag_2MoO_4 shown a superior photocatalytic efficacy over the commercial Ag_2MoO_4 and TiO_2 powder for the degradation of CIP solution.

Catalyst dosage is an important parameter that can significantly influence the rate of photodegradation. Figure 7C shows the efficiency of CIP degradation (%) against the effect of catalyst loading by varying the catalyst amount from 30 to 80 mg/mL, wherein the concentration of CIP and intensity of the light were maintained as constant. It can be seen that the rate of photocatalytic degradation was maximum at 50 mg/mL, due to the generation of more number of electron-hole pairs. However, the addition of excess amount of photocatalyst can blocks the existing active sites and interfere with the diffusion of photons. As a result, the photocatalytic degradation of CIP was decreased when increase the concentration of photocatalyst over 50 mg/mL[58].

Effect of initial concentration of CIP solution on the photodegradation was also investigated and the concentration varied from 10 to 30 mg/L under identical conditions, the results are shown in Fig. 7D. In the present case ~98% degradation was achieved at 20 mg/L whereas 83% and 77% degradation were observed at 25 and 30 mg/L concentration of CIP, respectively. This is due to the screening of light by the CIP solution and the less number of photons to reach the Ag_2MoO_4 surface. Hence, the electron-hole pair generation is reduced greatly and consequently, the degradation efficiency decreased.

Generally, the reactive oxidative species (ROS) *viz* hydroxyl radical (·OH), superoxide radical anion ($O_2^{\cdot -}$), hole (h^+) and electron (e^-) involved in the photocatalytic reaction[59]. The photocatalytic mechanism of the degradation of CIP is represented in the following equations

$$Ag_2MoO_4 + h\nu \rightarrow Ag_2MoO_4\ (e_{CB}^- + h_{VB}^+) \quad (1)$$

$$Ag_2MoO_4(e_{CB}^-) + O_2 \rightarrow Ag_2MoO_4 + O_2^{\cdot -} \quad (2)$$

$$Ag_2MoO_4(h_{VB}^+) + H_2O \rightarrow Ag_2MoO_4 + HO\cdot \quad (3)$$

$$O_2^{\cdot -} + H^+ \rightarrow \cdot HO_2 \quad (4)$$

$$HO\cdot, O_2^{\cdot -}, \cdot HO_2, + CIP \rightarrow CIP^{\cdot +} + H_2O \quad (5)$$

$$HO\cdot, O_2^{\cdot -}, \cdot HO_2, + CIP^{\cdot +} \rightarrow derivatives\ of\ CIP \rightarrow H_2O + CO_2 \quad (6)$$

The semiconductor photocatalyst generally undergoes excitation under light illumination with energy greater than the bandgap while the e^- excited from the valence band (VB) to the conduction band (CB) leaves h^+ in the VB[60]. In the present study, Ag_2MoO_4 was irradiated by UV light which produced the e^- in the CB and h^+ in the VB, as illustrated in the Eq. 1. The e^- in the CB were reacted with the oxygen molecule to form $O_2^{\cdot -}$ and the $O_2^{\cdot -}$ was reacted with the water molecule to form $\cdot HO_2$, as shown in Eqs 2 and 4. Furthermore, h^+ in the VB adsorbed water molecules and reacted to form ·OH, as given in Eq. 2. The ROS formed in the photocatalytic reaction facilitated the degradation of the CIP by the stepwise photocatalytic reduction process (Eqs 5 and 6).

The high photocatalytic activity as well as recycling ability of the catalyst is a vital issue for long-term use in practical applications. To evaluate the sustainability of Ag_2MoO_4, the recycling experiments were carried out for the degradation of CIP, as illustrated in Fig. 7E. The photocatalytic activity of the Ag_2MoO_4 on CIP degradation did not show a significant loss and attains more than 90% of degradation rate even after the five successive cycles with every cycle lasting for 40 min, which indicating that the potato-like Ag_2MoO_4 microstructure is a very effective and highly stable photocatalyst. Thus, the obtained results also indicated a good reusability of the catalyst. Moreover, the poor loss of catalytic activity during the recycle performance is due to the accumulation of impurities on the surfaces of the photocatalyst.

Electrochemical performance to hydrogen peroxide on Ag_2MoO_4 modified GCE. Cyclic voltammetry studies of the H_2O_2 sensor was demonstrated using bare GCE (a,c) and (b,d) Ag_2MoO_4 modified GCE in absence (curve a & b) and presence of 200 μM H_2O_2 (curve c & d) containing N_2 saturated 0.05 M PBS (pH 7) at a scan rate 50 mV/s. In the absence of H_2O_2 (curve a & b), the results clearly indicates that there is no significant reduction peak appeared in the selected potential window. Whereas, in the presence of 200 μM H_2O_2 on Ag_2MoO_4 modified GCE (curve d) shows a strong and higher reduction peak current appeared at the lower onset potential −0.26 V due to the catalytic behavior of Ag_2MoO_4. Although, we also observed a slight and not considerable reduction peak in the bare GCE at the longer potential −0.7 V (curve c). The reduction peak current of H_2O_2 on Ag_2MoO_4 modified GCE is 10 times much higher than that of bare GCE. The above results confirmed that Ag_2MoO_4 modified GCE has high catalytic ability for H_2O_2 detection. Consequently, Ag_2MoO_4 are suitable as mediators to transfer electron between H_2O_2 and working electrode and make possible electrochemical

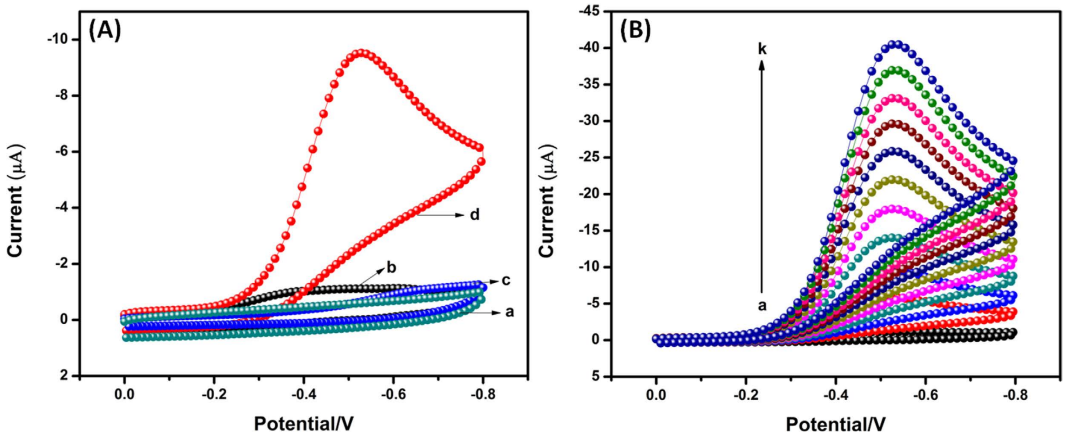

Figure 8. (**A**) Cyclic voltammograms for the reduction of H_2O_2 on bare GCE (a,c) and Ag_2MoO_4 modified GCE (b,d) in absence (a,b) and presence (c,d) of 200 μM H_2O_2 containing N_2 saturated 0.05 M PBS (pH 7) at a scan rate of 50 mV/s. (**B**) Cyclic voltammograms of Ag_2MoO_4 modified GCE in N_2 saturated 0.05 M PBS (pH 7) in the absence and presence of H_2O_2 with different concentrations (a–k: 0 to 1 mM) at a scan rate of 50 mV/s.

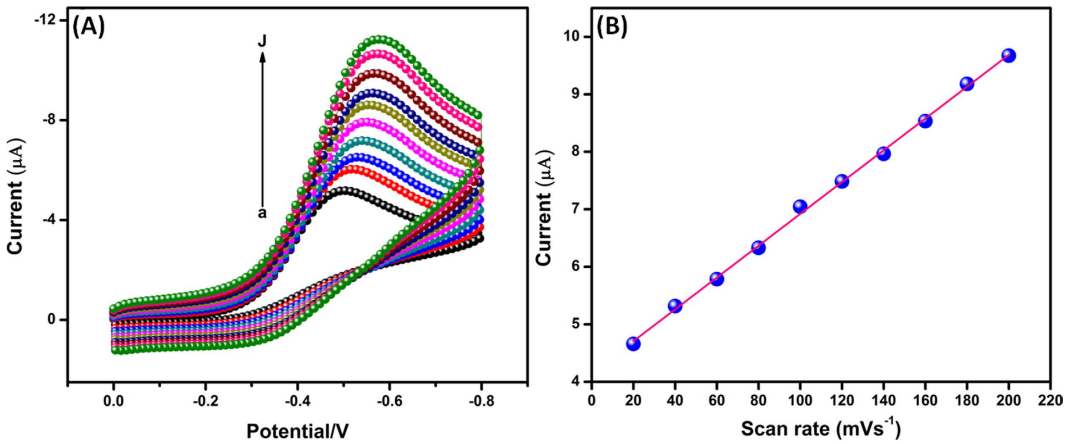

Figure 9. (**A**) Cyclic voltammograms of Ag_2MoO_4 modified electrode in 200 μM H_2O_2 containing N_2 saturated 0.05 M PBS (pH 7) at different scan rates from 20 to 200 mV/s (a–j) and (**B**) Corresponding calibration plot of scan rate vs. I_{pc} of H_2O_2.

regeneration following electron exchange with H_2O_2. The possible mechanisms for the electrochemical reduction of hydrogen peroxide as shown in Eqs (7–9). In order to investigate the electrocatalytic activity of Ag_2MoO_4 modified GCE, CVs were performed in the presence of different addition of H_2O_2 in 0.05 M PBS (pH 7), as shown in Fig. 8B. The reduction peak current of H_2O_2 was linearly increased with increasing the H_2O_2 concentration from 0 to 1 mM, which revealing electrocatalytic activity of Ag_2MoO_4 modified GCE toward the H_2O_2. Furthermore, the low level detection, sensitivity and linear range of H_2O_2 were clearly discussed in amperometric (*i-t*) section.

$$H_2O_2 + e^- \rightarrow OH_{ad} + OH^- \quad (7)$$

$$OH_{ad} + e^- \rightarrow OH^- \quad (8)$$

$$2OH^- + 2H^+ \rightarrow 2H_2O \quad (9)$$

Furthermore, the electrocatalytic behavior of the Ag_2MoO_4 modified GCE towards H_2O_2 was studied with the change of scan rate. Figure 9A reveals the CVs responses of 200 μM of H_2O_2 detection at Ag_2MoO_4/GCE with different scan rate ranges from 20 to 200 mV/s and its denoted (a–j). When increasing the scan rate from 20 to 200 mV/s, the reduction peak current of H_2O_2 was increased and the peak potential was shifted towards the more negative side. The peak current of H_2O_2 reduction is directly proportional to the scan rate (Fig. 9B) (Correlation co-efficient $R^2 = 0.998$), indicating that the electrode process is surface controlled process[61].

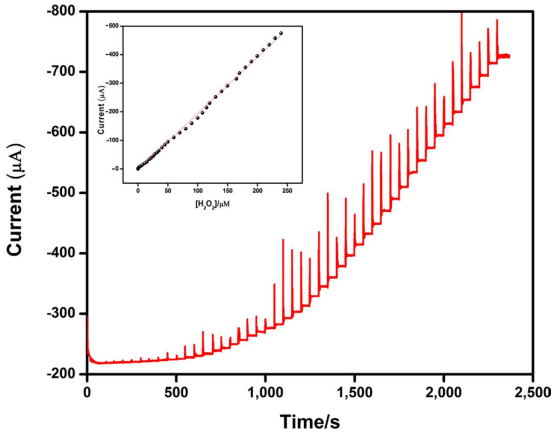

Figure 10. Amperometric *i–t* responses of H_2O_2 reduction at Ag_2MoO_4 film modified RDGCE upon successive additions of H_2O_2 from 0.04 to 247 μM into continuously stirred N_2 saturated 0.05 M PBS (pH 7). Applied potential: −0.5 V; Rotation rate: 1200 rpm. Inset shows the calibration plot of response current vs. H_2O_2 concentration [0.04–240 μM].

The effect of pH is very important phenomenon for the electrochemical sensor and biosensor. The electrocatalytic performance of Ag_2MoO_4 modified GCE for H_2O_2 reduction was examined in different pH solution. The CVs of Ag_2MoO_4 modified GCE in the presence of 200 μM H_2O_2 at different pH ranges (3 to 11) of 0.05 M PBS solution were studied and its calibration plot is depicted in Figure S1. When the pH value increased from 3 to 5, the reduction peak current increased and then decreased gradually while increasing the pH more than 7. However, higher peak currents are observed at pH 7. Therefore, Ag_2MoO_4 modified GCE has good electrocatalytic activity at pH 7 and the reduction of H_2O_2 is pH dependence. Therefore, we chosen pH 7 is optimized pH and this pH was used further electrochemical measurements.

Amperometric determination of H_2O_2 at Ag_2MoO_4 modified GCE. The amperometric *i-t* technique is one of the most important method to determine the electrocatalytic activity of modified electrodes in electrochemical sensor and biosensor applications. In the present work, we have utilized an amperometric method to estimate the performance of Ag_2MoO_4 modified GCE toward H_2O_2 detection. In this regards, Ag_2MoO_4 modified rotating disc glassy carbon electrode (RDGCE) was performed in continuously stirred pH 7 solution by applying constant potential at −0.5 V with rotation speed at 1200 rpm. Figure 10 reveals the amperometric *i-t* performance obtained at Ag_2MoO_4 modified RDGCE upon the different addition of H_2O_2 (0.049 to 247 μM) in the PBS solution. These results undoubtedly shows that Ag_2MoO_4 modified film demonstrates a fast and well-defined response obtained in each different addition of H_2O_2 concentration. The response time of H_2O_2 detection on Ag_2MoO_4 modified RDGCE was observed for 5 s, it's clearly suggesting that the fast electron movement process was occurred in the electrolyte and electrode interface when introducing the H_2O_2. The linear response current increases with increasing the concentration of H_2O_2 (low concentration to high concentration) from 0.049 to 240 μM (linear range inset; Fig. 10), the obtained sensitivity and limit of detection (LOD) of the sensor is around 9.8 $\mu A \mu M^{-1} cm^{-2}$ and 0.03 μM, respectively. The above results suggesting that the Ag_2MoO_4 modified RDGC electrode has good electrocatalytic activity towards H_2O_2. The analytical parameters, such as LOD, linear range, and sensitivity, of H_2O_2 sensor was compared with various modified electrodes are summarized in Table 1. Clearly, the Ag_2MoO_4 modified RDGCE, reported here, exhibits good sensitivity and LOD over a wide linear range of H_2O_2 concentration compared to other reports[62–75].

Selectivity is very important study in the electrochemical sensor. In order to investigate selectivity, the proposed sensor was used to detect the H_2O_2 in the presence of variety of biological interferences such as catechol (b), fructose (c), lactose (d), sucrose (e), glucose (f), hydroquinone (g), ascorbic acid (h), uric acid (i), dopamine (j) and epinephrine (k) with 50-fold excess concentration of each analytes, as shown in Fig. 11. The Ag_2MoO_4 modified RDGCE exhibited well-defined response towards each 100 μM H_2O_2 (a). No remarkable responses were monitored for the 50-fold excess concentration of biological interferences as mentioned above. Hence, the Ag_2MoO_4 modified RDGCE has excellent selectivity towards the determination of H_2O_2. Furthermore, we have studied the stability of our proposed sensor by amperometric (*i-t*) techniques and the results obtained as it can be seen in Figure S2. The prepared sensor retains its 98.2% of its initial response of H_2O_2 after prolongs runs up to 2600 s, which suggesting the good stability of the sensor.

In summary, a potato-like Ag_2MoO_4 microparticles were successfully prepared through a simple hydrothermal method. Different analytical and spectroscopic methods were used to confirm the structural nature of Ag_2MoO_4 microparticles. All the obtained results are strongly evidenced that the prepared compound shows like pristine Ag_2MoO_4 without any other impurities. The as-prepared Ag_2MoO_4 microparticles explored excellent photocatalytic activity towards the degradation of chronic toxicity CIP under UV-light illumination and 98% of the CIP was degraded within 40 min. On the other hand, the Ag_2MoO_4 microparticles were used to fabricate the sensor electrode for the detection of H_2O_2 in the potentially interfering biological substances. The Ag_2MoO_4 modified GCE revealed a high electrocatalytic activity with wide linear range, good stability and low detection limit than the previous reports. Finally, the Ag_2MoO_4 represents an interesting and promising candidate for photocatalytic

Modified electrode	Method of detection	LR (μM)	LOD (μM)	Ref.
AgNPs/DNA/GCE	Amperometry	2.0–2500	0.6	62
GNs/Ag/GCE	Amperometry	100.0–40,000	28.0	63
AgNWs/CS/GCE	Amperometry	8.0–1350	2.0	64
AgNWs/PtE	Amperometry	0.5–3000	0.2	65
ZnONRs/AgNPs/GCE	Amperometry	0.9–983.0	0.9	66
SiNWs/AgNPs/GCE	Amperometry	0.2 −20,000	0.2	67
AgNPs/GCE	Amperometry	4.0–60.0	1.3	68
PVP–AgNWs/GCE	Amperometry	20.0–3620	2.3	69
GR/AgNWs/GCE	Amperometry	1	1.0	70
CNT/AgNPs/GCE	Amperometry	9.0–9000	1.6	71
RGO/AgNPs/GCE	Amperometry	100.0–8000	7.1	72
Ag/GCE	Amperometry	5.0–12,000	0.5	73
Ag-AlOOH-rGO	Amperometry	5.0 to 4200	1.8	74
Ag-Bt/GCE	Amperometry	—	9.1	75
Ag_2MoO_4/GCE	Amperometry	0.04–240	0.03	This work

Table 1. Comparison of analytical performance of Ag_2MoO_4 modified electrode with previously reported similar modified electrodes for the detection of H_2O_2. Abbreviations: LR–linear response range; LOD–limit of detection; NPs–nanoparticles; NWs–nanowires; Ag- Silver nanoparticles; CS–chitosan; GCE–glassy carbon electrode; GR–graphene; PVP–polyvinylpyrolidone; GNs–graphene nanosheets; PtE–platinum electrode; CNT–carbon nanotubes; NRs–nanorods; RGO–reduced graphene oxide; AlOOH- Aluminum oxyhydroxide: Ag-Bt- silver nanoparticle-incorporated bentonite clay.

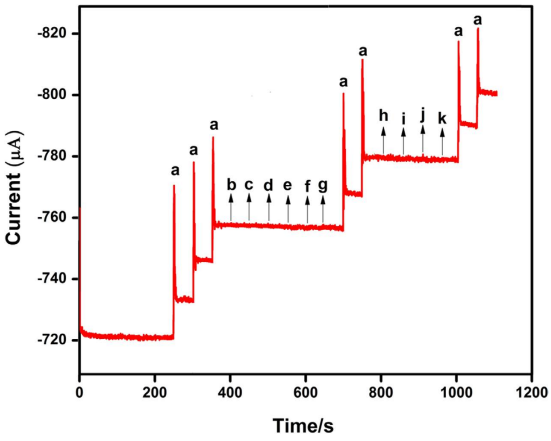

Figure 11. Amperometric *i–t* responses of H_2O_2 reduction at Ag_2MoO_4 modified RDGCE for the successive addition of 100 μM of H_2O_2 (**a**), and 50-fold excess concentration of catechol (**b**), fructose (**c**), lactose (**d**), sucrose (**e**), glucose (**f**), hydroquinone (**g**), ascorbic acid (**h**), uric acid (**i**), dopamine (**j**) and epinephrine (**k**) in continuously stirred N_2 saturated 0.05 M PBS (pH 7). Applied potential: −0.5 V; Rotation rate: 1200 rpm.

and electrochemical applications with the advantages of one-pot preparation, unique features, excellent catalytic activity and high sensing performance.

Experimental Section

Materials. Silver nitrate ($AgNO_3$), sodium molybdate dihydrate ($Na_2MoO_4.2H_2O$), urea (CH_4N_2O), hydrogen peroxide (H_2O_2) and all chemicals were purchased from Sigma-Aldrich and used further purification. Ciprofloxacin drug was purchased from Thiruvengadam Medicals, Virudhunagar, India. All other chemicals were of analytical grade and used without further purification. The phosphate buffer solution (PBS) was prepared using 0.05 M Na_2HPO_4 and NaH_2PO_4 and all the required solutions were prepared using deionized water (DI).

Synthesis of silver molybdate. In a typical synthesis, 0.5 M of $Na_2MoO_4.2H_2O$ and 0.1 M of $AgNO_3$ were dissolved in 60 mL DI water. Then, 0.3 g of urea (10 mL) was gradually added into the above mixture under vigorous stirring at room temperature for 30 min. The mixture was transferred into 100 mL Teflon-lined autoclave and maintained at 120 °C for 8 h in an oven. The autoclave was then cooled down to room temperature naturally, and the obtained yellow product was collected by centrifugation and washed thoroughly with DI water and ethanol for three times and dried overnight at 80 °C.

Characterization. The powder X-ray diffraction (XRD) analysis was carried out using PANalytical X'Pert PRO X-ray diffractometer measured with Cu-Kα radiation ($\lambda = 1.54178$ Å) in the 2θ range of 10–100°. X-ray photoelectron spectroscopy (XPS) measurements were carried out using ULVAC-PHI 5000 VersaProb instrument. Scanning electron microscope (SEM) and Energy dispersive X-ray spectra (EDX) were probed using Hitachi S-3000 H and HORIBA EMAX X-ACT, respectively. Raman spectra were collected in an NT-MDT confocal Raman microscopic system with an exciting laser wavelength of 488 nm and the laser spot-size is around 0.5 μm. Fourier transform infrared spectroscopy (FTIR) was recorded by Shimadzu FT-IR 3000 spectrometer in the diffuse reflectance mode at a resolution of 4 cm^{-1}, the sample was pressed into KBr disc with a weight ratio of sample to KBr of 1:100 in the range of 4000-400 cm^{-1}. UV-Visible diffused reflectance (DRS) spectrum of the sample was taken from Shimadzu UV-2600 spectrophotometer and $BaSO_4$ was used as a reflectance reference material. The absorption spectra in the photocatalytic degradation process were monitored by Shimadzu 2100 UV-Visible spectrometer. The electrochemical impedance spectroscopy (EIS) was performed by XPOT (ZAHNER elektrik instrument). Cyclic voltammetry (CV) and Amperometric (*i-t*) experiments were carried out using CHI 405a work station and PINE instrument, respectively. All the electrochemical studies were carried out in three-electrode cell system, glassy carbon electrode (GCE surface area = 0.071 cm^2) was used as a working electrode, platinum wire and standard Ag/AgCl electrodes were used as a counter and reference electrode, respectively.

Photocatalytic activity. The photocatalytic activity of the as-prepared Ag_2MoO_4 was evaluated via degradation of CIP solution under UV light illumination ($\lambda = 200$~400 nm). In a typical activity, 50 mg/mL of catalyst was dispersed in 100 mL aqueous solutions of CIP (20 mg/L). Prior to illumination, the solution mixture was stirred magnetically for 30 min in the dark to establish the adsorption-desorption equilibrium between CIP and as-prepared Ag_2MoO_4 photocatalyst. Then, the solutions were illuminated by UV light ($\lambda_{max} = 365$ nm) to induce photocatalytic reaction. During the irradiation, 5 mL of the solution was withdrawn at 5 min time intervals and centrifuged to remove the catalyst. The obtained clear liquor was analyzed by UV-Vis spectrometer to determine the concentration changes of CIP.

Fabrication of silver molybdate modified GCE. Before surface modification, the GCE was mirror like polished with 0.05 μm alumina slurry and rinsed with DI to remove the alumina particles on the GCE surface. After that the GCE was sonicated for 1 min containing ethanol and water (1:1 ratio). About 5 mg/mL of the as-prepared Ag_2MoO_4 was re-dispersed in DI water and about 8 μL (optimized concentration) of the dispersed Ag_2MoO_4 was drop casted on the GCE surface. Then it was allowed to dry at room temperature, followed by the dried Ag_2MoO_4 modified GCE was rinsed with DI water to remove the loosely attached catalyst on the GCE surface. The obtained Ag_2MoO_4 modified GCE was used to further electrochemical experiments. Then, it was stored in room temperature when not in use.

References

1. Glassmeyer, S. T. *et al.* Transport of chemical and microbial compounds from known wastewater discharges: Potential for use as indicators of human fecal contamination. *Environ. Sci. Technol.* **39,** 5157–5169 (2005).
2. Beier, S. *et al.* Treatment of hospital wastewater effluent by nanofiltration and reverse osmosis. *Water Sci. Technol.* **61,** 1691–1698 (2010).
3. Wei, X. Y. *et al.* Advanced treatment of a complex pharmaceutical wastewater by nanofiltration: Membrane foulant identification and cleaning. *Desalination*. **251,** 167–175 (2010).
4. Dodd, M. C., Shah, A. D., Von Gunten, U. & Huang, C. H. Interactions of fluoroquinolone antibacterial agents with aqueous chlorine: reaction kinetics, mechanisms, and transformation pathways. *Environ. Sci. Technol.* **39,** 7065–7076 (2005).
5. Carlsson, G., Orn, S. & Larsson, D. G. J. Effluent from bulk drug production is toxic to aquatic vertebrates. *Environ. Toxicol. Chem.* **28,** 2656–2662 (2009).
6. Aristilde, L., Melis, A. & Sposito, G. Inhibition of Photosynthesis by a Fluoroquinolone Antibiotic. *Environ. Sci. Technol.* **44,** 1444–1450 (2010).
7. Belden, J. B., Maul, J. D. & Lydy, M. J. Partitioning and photodegradation of ciprofloxacin in aqueous systems in the presence of organic matter. *Chemosphere*. **66,** 1390–1395 (2007).
8. Tan, Y. Y., Guo, Y., Gu, X. Y. & Gu, C. Effects of metal cations and fulvic acid on the adsorption of ciprofloxacin onto goethite. *Environ. Sci. Pollut. Res*. **22,** 609–617 (2015).
9. Wang, P., He, Y. L. & Huang, C. H. Oxidation of fluoroquinolone antibiotics and structurally related amines by chlorine dioxide: reaction kinetics, product and pathway evaluation. *Water Res*. **44,** 5989–5998 (2010).
10. De Bel, E., Dewulf, J., Van Lagenhove, H. & Janssen, C. Influence of pH on the sonolysis of ciprofloxacin: biodegradability, ecotoxicity and antibiotic activity of its degradation products. *Chemosphere*. **77,** 291–295 (2009).
11. Chen, H., Gao, B. & Li, H. Removal of sulfamethoxazole and ciprofloxacin from aqueous solutions by graphene oxide. *J. Hazard. Mater*. **282,** 201–207 (2015).
12. De Lima Perini, J. A., Perez-Moya, M. & Nogueira, R. F. P. Photo-Fenton degradation kinetics of low ciprofloxacin concentration using different iron sources and pH. *J. Photochem. Photobiol. A*. **259,** 53–58 (2013).
13. El-Kemary, M., El-Shamy, H. & El-Mehasseb, I. Photocatalytic degradation of ciprofloxacin drug in water using ZnO nanoparticles. *J. Lumin*. **130,** 2327–2331 (2010).
14. Jiang, Z. *et al. In situ* synthesis of bimetallic Ag/Pt loaded single-crystalline anatase TiO_2 hollow nano-hemispheres and their improved photocatalytic properties. *Cryst Eng Comm*. **16,** 2384–2394 (2014).
15. Jiang, Z. *et al.* Natural leaves assisted synthesis of nitrogen-doped, carbon-rich nanodots sensitized, Ag-loaded anatase TiO_2 square nanosheets with dominant 001 facets and their enhanced catalytic applications. *J. Mater. Chem. A*. **47,** 14963–14972 (2013).
16. Sui, M. H. *et al.* Heterogeneous catalytic ozonation of ciprofloxacin in water with carbon nanotube supported manganese oxides as catalyst. *J. Hazard. Mater*. **227–228,** 227–236 (2012).
17. Zangeneh, H. *et al.* Photocatalytic oxidation of organic dyes and pollutants in wastewater using different modified titanium dioxides: a comparative review. *J. Ind. Eng. Chem*. **26,** 1–36 (2015).
18. Byrne, J. A. *et al.* A review of heterogeneous photocatalysis for water and surface disinfection. *Molecules*. **20,** 5574–5615 (2015).
19. Miller, E. W. *et al.* Boronate-Based Fluorescent Probes for Imaging Cellular Hydrogen Peroxide. *J. Am. Chem. Soc.* **127,** 16652–16659 (2005).
20. Rhee, S. G. H_2O_2, a Necessary Evil for Cell Signaling. *Science*. **312,** 1882–1883 (2006).

21. Penkett, S. A., Jones, B. M. R., Brice, K. A. & Eggleton, A. E. J. The importance of atmospheric ozone and hydrogen peroxide in oxidising sulphur dioxide in cloud and rainwater. *Atmos. Environ*. **41,** 154–168 (2007).
22. Laloi, C., Apel, K. & Danon, A. Reactive oxygen signalling: the latest news. *Curr. Opin. Plant Biol*. **7,** 323–328 (2004).
23. Karuppiah, C. *et al.* An Ultrahigh Selective and Sensitive Enzyme-Free Hydrogen Peroxide Sensor Based on Palladium Nanoparticles and Nafion-Modified Electrode. *Electrocatalysis*. **5,** 177–185 (2014).
24. Xiao, W. *et al.* Synthesis, Characterization, and Lithium Storage Capability of AMoO4 (A = Ni, Co) Nanorods. *Chem. Mater*. **22,** 746–754 (2010).
25. Tournois, P. Acousto-optic programmable dispersive filter for adaptive compensation of group delay time dispersion in laser systems. *Opt. Commun*. **140,** 245–249 (1997).
26. Zhang, Z. *et al.* Facile hydrothermal synthesis of $NiMoO_4$@$CoMoO_4$ hierarchical nanospheres for supercapacitor applications. *Phys Chem Chem Phys*. **17,** 20795–20804 (2015).
27. Senthilkumar, B. *et al.* Nano α-$NiMoO_4$ as a new electrode for electrochemical supercapacitors. *RSC Adv*. **3,** 352–357 (2013).
28. Rushbrooke, J. G. & Ansorge, R. E. Optical Fiber Readout and Performance of Small Scintillating Crystals for a Fine- Grained Gamma Detector. Nucl. Instrum. *Methods Phys.Res. Sect A*. **280,** 83–90 (1989).
29. Ryu, J. H. *et al.* Microwave-assisted synthesis of $CaMoO_4$ nano-powders by a citrate complex method and its photoluminescence property. *J. Alloys Compd*. **390,** 245–249 (2005).
30. Mikhailik, V. B. & Kraus, H. Performance of scintillation materials at cryogenic temperatures. *Phys. Status Solidi. B*. **247,** 1583–1599 (2010).
31. Nasab, A. S., Maddahfar, M. & Mashkani, S. M. H. $Ce(MoO4)_2$ nanostructures: Synthesis, characterization, and its photocatalyst application through the ultrasonic method. *J. Mol. Liq*. **216,** 1–5 (2016).
32. Shen, M. *et al.* Hierarchical $PbMoO_4$ microspheres: hydrothermal synthesis, formation mechanism and photocatalytic properties. *Cryst Eng Comm*. **15,** 1146–1152 (2013).
33. Sundaram, R. & Nagaraja, K. S. Solid state electrical conductivity and humidity sensing studies on metal molybdate–molybdenum trioxide composites ($M = Ni^{2+}$, Cu^{2+} and $^{Pb2+}$). *Sens. Actuators B*. **101,** 353–360 (2004).
34. Ding, Y., Yu, S. H., Liu, C. & Zang, Z. A. 3D Architectures of Iron Molybdate: Phase Selective Synthesis, Growth Mechanism, and Magnetic Properties. *Chem. Eur*. J. **13,** 746–753 (2007).
35. Driscoll, S. & Ozkan, U. S. Effect of O_2 Concentration in Selective and Complete Oxidation of 1,3-Butadiene, Furan, and Maleic Anhydride over $MnMoO_4/MoO_3$ Catalysts. *Stud. Surf. Sci. Catal*. **82,** 367–375 (1994).
36. Cunha, F. S. *et al.* Structural, morphological and optical investigation of β-Ag_2MoO_4 microcrystals obtained with different polar solvents. *Cryst Eng Comm*. **17,** 8207–8211 (2015).
37. Bhattacharya, S. & Ghosh, A. Silver molybdate nanoparticles, nanowires, and nanorods embedded in glass nanocomposites. *Phys Rev B*. **75,** 092103 (2007).
38. Arora, A. K., Nithya, R., Misra, S. & Yagi, T. Behavior of silver molybdate at high-pressure. *J. Solid State Chem*. **196,** 391–397 (2012).
39. Misra, S., Jayaraman, V. & Gnanasekaran, T. Trace Level Gas Sensing Characteristics of Nano-Crystalline Silver Decamolybdate. *Soft Nanosci. Lett*. **3,** 39–42 (2013).
40. Tang, H. *et al.* Highly antibacterial materials constructed from silver molybdate nanoparticles immobilized in chitin matrix. *Chem. Eng. J*. **234,** 124–131 (2013).
41. Cheng, L. *et al.* Photoswitches of one-dimensional Ag_2MO_4 (M = Cr, Mo, and W). *J. Phys. Chem. C*. **113,** 1764–1768 (2009).
42. Zhou, D. *et al.* Sintering Behavior and Dielectric Properties of Ultra-Low Temperature Fired Silver Molybdate Ceramics. *J. Am. Ceram. Soc*. **97,** 3597–3601 (2014).
43. Bai, Y., Lu, Y. & Liu, J. K. An efficient photocatalyst for degradation of various organic dyes: Ag@Ag_2MoO_4-AgBr composite. *J. Hazard. Mater*. **307,** 26–35 (2016).
44. ZhaoQian, L., XueTai, C. & Ling, X. Z. Microwave-assisted hydrothermal synthesis of cube-like Ag-Ag_2MoO_4 with visible-light photocatalytic activity. *Sci. China. Chem*. **56,** 443–450 (2013).
45. Feng, M. *et al.* Ultralong Silver Trimolybdate Nanowires: Synthesis, Phase Transformation, Stability, and Their Photocatalytic, Optical, and Electrical Properties. *ACS Nano*. **5,** 6726–6735 (2011).
46. Nagaraju, G., Chandrappa, G. T. & Livage, J. Synthesis and characterization of silver molybdate nanowires, nanorods and multipods. *Bull. Mater. Sci*. **31,** 367–371 (2008).
47. Saito, K. *et al.* Monoclinic $Ag_2Mo_2O_7$ nanowire: a new Ag-Mo-O nanophotocatalyst material. *Inorg. Chem*. **52,** 8297–8299 (2013).
48. Jiang, H. *et al.* Thermal perturbation nucleation and growth of silver molybdate nanoclusters by a dynamic template route. *Cryst Eng Comm*. **17,** 5511–5521 (2015).
49. Singh, D. P. *et al.* Broom-like and flower-like heterostructures of silver molybdate through pH controlled self assembly. *J. Nanopart. Res*. **14,** 660–671 (2012).
50. Fabbro, M. T. *et al.* Identifying and rationalizing the morphological, structural, and optical properties of β-Ag_2MoO_4 microcrystals, and the formation process of Ag nanoparticles on their surfaces: combining experimental data and first-principles calculations. *Sci. Technol. Adv. Mater.* **16,** 065002 (1–10) (2015).
51. Juan, A. *et al.* A combined experimental and theorectical study on the formation of Ag filaments on β-Ag_2MoO_4 induced by electron irradiation. *Part. Part. Syst. Charact*. **32,** 646–651 (2015).
52. Saravanakumar, K., Ramjan, M. M., Suresh, P. & Muthuraj, V. Fabrication of highly efficient visible light driven Ag/CeO_2 photocatalyst for degradation of organic pollutants. *J. Alloy. Compd*. **664,** 149–160 (2016).
53. Subcik, J. *et al.* Structure and properties of MoO_3-containing zinc borophosphate glasses. *J Non-Cryst Solids*. **355,** 970–975 (2009).
54. Arora, A. K. Amorphization and decomposition of scandium molybdate at high pressure. *J. Apply. Phys*. **97,** 013508 (2005).
55. Jiang, Z. & Xie, J. *In-situ* growth of Ag/Ag_2O nanoparticles on g-C_3N_4 by a natural carbon nanodots-assisted green method for synergistic photocatalytic activity. *RSC Adv*. **6,** 3186–3197 (2016).
56. Xu, Z. *et al.* Supercapacitive carbon nanotube-cobalt molybdate nanocomposites prepared via solvent-free microwave synthesis. *RSC Adv*. **2,** 2753–2755 (2012).
57. Yang, L. *et al.* Structure and effective visible-light-driven photocatalytic activity of α-$NiMoO_4$ for degradation of methylene blue dye. *J. Alloys Compd*. **664,** 756–763 (2016).
58. Chowdhury, P. R. & Bhattacharyya, K. G. Ni/Ti layered double hydroxide: synthesis, characterization and application as a photocatalyst for visible light degradation of aqueous methylene blue. *Dalton Trans*. **44,** 6809–6824 (2015).
59. Li, Z., Cong, S. & Xu, Y., Brookite vs Anatase TiO_2 in the Photocatalytic Activity for Organic Degradation in Water. *ACS Catal*. **4,** 3273–3280 (2014).
60. Kumar, P. S. *et al.* Novel CuO/chitosan nanocomposite thin film: facile hand-picking recoverable, efficient and reusable heterogeneous photocatalyst. *RSC Adv*. **5,** 57493–57501 (2015).
61. Fotouhi, L., Fatollahzadeh, M. & Heravi, M. M. Electrochemical Behavior and Voltammetric Determination of Sulfaguanidine at a Glassy Carbon Electrode Modified With a Multi-Walled Carbon Nanotube. *Int. J. Electrochem. Sci*. **7,** 3919–3928 (2012).
62. Wu, S. *et al.* Electrodeposition of silver–DNA hybrid nanoparticles for electrochemical sensing of hydrogen peroxide and glucose. *Electrochem. Commun*. **8,** 1197–1203 (2006).
63. Liu, S. *et al.* Stable Aqueous Dispersion of Graphene Nanosheets: Noncovalent Functionalization by a Polymeric Reducing Agent and Their Subsequent Decoration with Ag Nanoparticles for Enzymeless Hydrogen Peroxide Detection. *Macromolecules*. **43,** 10078–10083 (2010).

64. Gao, X. *et al.* A Nonenzymatic Hydrogen Peroxide Sensor Based on Silver Nanowires and Chitosan Film. *Electroanal*. **24,** 1771–1777 (2012).
65. Qin, X. *et al.* A novel non-enzyme hydrogen peroxide sensor based on catalytic reduction property of silver nanowires. *Talanta*. **139,** 56–61 (2015).
66. Lin, C. Y. *et al.* Electrode modified with a composite film of ZnO nanorods and Ag nanoparticles as a sensor for hydrogen peroxide. *Talanta*. **82,** 340–347 (2010).
67. Yin, J. *et al.* A hydrogen peroxide electrochemical sensor based on silver nanoparticles decorated silicon nanowire arrays. *Electrochim. Acta.* **56,** 3884–3889 (2011).
68. Liao, K. *et al.* A promising method for fabricating Ag nanoparticle modified non-enzyme hydrogen peroxide sensors. *Sens. Actuators B*. **181,** 125–129 (2013).
69. Yang, X. *et al.* Hydrogen peroxide and glucose biosensor based on silver nanowires synthesized by polyol process. *Analyst*. **137,** 4362–4367 (2012).
70. Zhang, M. & Wang, Z. Nanostructured silver nanowires-graphene hybrids for enhanced electrochemical detection of hydrogen peroxide. *Appl. Phys. Lett.* **102,** 213104 (2013).
71. Shi, Y. *et al.* Carbon nanotube decorated with silver nanoparticles via noncovalent interaction for a novel nonenzymatic sensor towards hydrogen peroxide reduction. *J. Electroanal. Chem*. **656,** 29–33 (2011).
72. Liu, S. *et al.* Aniline as a dispersing and stabilizing agent for reduced graphene oxide and its subsequent decoration with Ag nanoparticles for enzymeless hydrogen peroxide detection. *J. Colloid Interface Sci*. **363,** 615–619 (2011).
73. Qin, X. *et al.* Synthesis of dendritic silver nanostructures and their application in hydrogen peroxide electro reduction. *Electrochim. Acta.* **56,** 3170–3174 (2011).
74. Ziyin, Y. *et al.* Sensing hydrogen peroxide with a glassy carbon electrode modified with silver nanoparticles, AlOOH and reduced graphene oxide. *Microchim. Acta*. **183,** 1131–1136 (2016).
75. Dharmendra, K. Y. *et al.* Electrochemical sensing platform for hydrogen peroxide determination at low reduction potential using silver nanoparticle-incorporated bentonite clay. *J. Appl. Electrochem.* **46,** 103–112 (2016).

Acknowledgements

Financial supports of this work by the Ministry of Science and Technology, Taiwan (NSC101-2113-M-027- 001-MY3 to SMC) are gratefully acknowledged. We are grateful to thank the University of Grant Commission (UGC-F. No. 42-348/2013 (SR) & 01.04.2013), New Delhi, India. We also express our gratitude to the College Managing Board, Principal and Head of the Department of Chemistry, VHNSN College, Virudhunagar for providing research facilities.

Author Contributions

J.V.K. and V.M. conceived the synthesis method and fabricated the Ag_2MoO_4 samples. They also performed photocatalytic activity and characterization of the materials and composed the manuscript. R.K. and S.-M.C. performed the electrochemical studies, analyzed the data and wrote the manuscript. C.K. performed the material characterization using XPS and Raman spectroscopy and also corrected the manuscript. S.-M.C. and V.M. supervised and finalized the project. All authors discussed the results and contributed to the final paper.

Additional Information

Supplementary information accompanies this paper at http://www.nature.com/srep

Competing financial interests: The authors declare no competing financial interests.

How to cite this article: Kumar, J. V. *et al.* Fabrication of potato-like silver molybdate microstructures for photocatalytic degradation of chronic toxicity ciprofloxacin and highly selective electrochemical detection of H_2O_2. *Sci. Rep.* **6**, 34149; doi: 10.1038/srep34149 (2016).